EUROFUSION WP19ER-CPR(20) 26729

D Papadakis et al.

The competing effects of temperature and neutron irradiation on the mechanical properties and microstructure of forged tungsten bar

Preprint of Paper to be submitted for publication in Special Issue of 31st Symposium on Fusion Technology (SOFT2020)

This work has been carried out within the framework of the EUROfusion Consortium and has received funding from the Euratom research and training programme 2014-2018 and 2019-2020 under grant agreement No 633053. The views and opinions expressed herein do not necessarily reflect those of the European Commission.

The competing effects of temperature and neutron irradiation on the microstructure and mechanical properties of ITER grade tungsten

D. Papadakis[1,2], S. Dellis[1], K. Mergia[1,*], D. Terentyev[3], G. Bonny[3], A. Dubinko[3], W. Van Renterghem[3], M. Konstantinovic[3] and S. Messoloras[1]

[1] Institute of Nuclear and Radiological Sciences and Technology, Energy and Safety, NCSR "Demokritos", Athens, 15310, Greece

[2] Department of Physics, School of Sciences, University of Athens, Athens, 15772, Greece

[4] SCK CEN, Nuclear Materials Science Institute, Boeretang 200, 2400 Mol, Belgium

Abstract

Within EUROfusion project a neutron irradiation campaign and post-irradiation characterization of tungsten (W) materials was initiated to advance the understanding of the basic phenomena underlying the neutron irradiation effects and provide experimental validation of theoretical models. Among tungsten materials double forged W in bar form (ITER grade) was selected because a) the microstructural modification induced by forging aims to reduce its ductile to brittle transition temperature down to room temperature and to improve its strength and b) of its technological interest for ITER. As neutron irradiations imitating fusion plant conditions are made at high temperatures, it is important to separate the effects arising from annealing from those induced by neutron irradiation. To this end, in the current work structural and mechanical characteristics of double forged W bar annealed at 1200 ^{o}C are compared to a neutron irradiated one at 0.18 dpa at 1200 ^{o}C. The neutron irradiation was carried out in the Belgian Material Test Reactor (BR2). Positron annihilation lifetime and Doppler broadening spectroscopy (PAS) is employed to characterize open volume defects; X-ray diffraction and Transmission Electron Microscopy (TEM) to assess texture and microstructure, respectively. Depth sensing instrumented indentation and impulse excitation technique are used to determine the mechanical and elastic properties, respectively. Annealing on its own reduces the hardness by 4% and increases the maximum creep depth by 13%, while irradiation at the same temperature significantly increases hardness by 20% and decreases the maximum creep depth by 15%. Both the elastic modulus and shear modulus decrease by about 4% with irradiation while annealing increases their values by about 4%. Texture effects are observed only after neutron irradiation. These findings are discussed in correlation with the formation of voids and dislocations loops observed by TEM and small and large vacancy clusters observed by PAS.

Keywords: Tungsten, Neutron irradiation, Positron Annihilation Spectroscopy, Transmission Electron Microscopy, Mechanical properties, Indentation

[*] Corresponding author: Konstantina Mergia, kmergia@ipta.demokritos.gr

1 Introduction

Tungsten (W) is the main candidate material for plasma-facing components for current and future fusion devices due to its high melting temperature, thermal conductivity, low tritium retention, good sputtering resistance, low swelling, thermal stress and shock resistance, and high-temperature strength [1, 2, 3, 4]. However, the high ductile to brittle transition temperature (DBTT) of tungsten, ranging from room temperature up to several hundred degrees Celsius, remains a major drawback for its full exploitation [2].

Within EUROfusion project a neutron irradiation campaign and post-irradiation characterization of W materials was initiated to advance the understanding of the basic phenomena underlying the neutron irradiation effects and provide experimental validation of theoretical models. Among tungsten materials double forged W in bar form was selected because forging is one of the proposed methods of microstructural modification for decreasing DBTT down to room temperature and to improve its strength [5, 6, 7, 8]. Furthermore, double forged W bar is considered as an ITER grade material to be used as a reference to other material options [2, 9, 10, 11, 12], while its use in the divertor of the DEMO fusion reactor is being investigated [13].

In order to assess the viability of W as a plasma facing material in a neutron environment, fission neutron irradiation at high temperature has been employed. The primary induced damage and the subsequent collision cascade of the primary knock-on atoms (PKA) result in extensive damage in the material appearing in the form of vacancy clusters or voids and dislocation loops [14, 15, 16]. In addition, absorption of neutrons from W nuclei leads to the formation of transmutation products, namely Rhenium (Re), Osmium (Os), and Tantalum (Ta) [17] impurity atoms which may form W-Re-Os precipitates [18]. The type and the population of induced defects are dictated by the neutron irradiation conditions, namely irradiation dose and irradiation temperature [19, 20, 21, 22, 23, 24]. Thus, knowledge of the effect of high-temperature heat treatment on W is important for the understanding of the defects' evolution mechanism.

High-temperature treatment can affect the microstructure of W through three processes, recovery, recrystallization, and grain growth and the study of the kinetics of these processes is the topic of several papers. L. Tanure *et al.* [25] studied the influence of isochronal (1 h) thermal treatment of double forged W bar and showed that recovery (sub-grain coarsening and/or sub-grain/dislocation reorientation) occurs at temperatures lower than 1300 ^{o}C, recrystallization between 1300 and 1500 ^{o}C and grain growth above 1500 ^{o}C. However, for prolonged periods of heat treatment lower temperatures are expected to trigger the same results [26, 27]. Alfonso *et. al.* [28] studied the influence of heat treatment on warm-rolled tungsten in the temperature range from 1150 ^{o}C to 1350 ^{o}C for an annealing period of up to 2200 h. In all the investigated temperatures two annealing stages were identified. In the first stage, recovery occurs while in the second stage recovery and recrystallization appear simultaneously. The increase of the annealing temperature lowers the time onset of the interchange between the first and the second stage. Tungsten's initial microstructure plays also a significant role in its behaviour under high-temperature heat treatment with even small changes inducing significant difference in the recovery and recrystallization kinetics as M. Richou *et al.* present in their paper [29].

In this work, the mechanical properties, texture, and microstructure of neutron-irradiated up to 0.18 dpa at 1200 ^{o}C double forged W bar are compared to those of an unirradiated and annealed at 1200 ^{o}C material. This comparison will enable the separation of the effects arising due to temperature from those induced by neutron irradiation and thus, get a better insight into the mechanism of the evolution of defects. X-ray diffraction (XRD) and Transmission Electron Microscopy (TEM) are used to assess texture and microstructure. Impulse excitation technique (IET) is employed to study the elastic properties of the specimens while depth-sensing micro-indentation is used to measure their hardness and creep. Positron annihilation lifetime and Doppler broadening spectroscopy (PAS) is employed to characterise open volume defects.

2 Materials and Methods

2.1 Material, annealing and irradiation

The tungsten material was produced by PLANSEE SE in bar form using a powder metallurgical route consisting of sintering and hot forging from two orthogonal directions. The resulting material has a uniaxial elongated grain shape [30, 31]. Disks with thickness of about 1 mm were sectioned using electrical discharge machining. Both sides of the discs were subsequently mechanically polished using diamond suspension up to 0.25 µm and colloidal silica in order to obtain mirror quality surface and removing surface oxide and stresses/surface damage induced by the EDM cutting. The final thickness of the samples was about 0.5 mm.

Neutron irradiation was performed at the Belgian Material Test Reactor BR2. In order to maximize the fast-to-thermal neutron ratio and thus achieving transmutation rates of W into Re and Os closer to those expected in ITER and DEMO, the irradiation was performed inside a fuel element in the maximum fast neutron (> 0.1 MeV, 7×10^{14} n/cm^2/s) flux position.

The samples were encapsulated in 1.5 mm stainless steel tube filled with helium. The thickness of the steel tube was adjusted to maximize the shielding from the thermal neutrons. The gap between the samples and the tube was adjusted to achieve 1200 $^{\circ}$C following the thermal and neutronic calculations. The irradiation was made for two reactor cycles of a total duration of 70 days resulting in a dose of 0.18 displacements per atom (dpa). The dose was calculated by MCNPX 2.7.0 based on the total fast neutron fluence (8.9×10^{20} n/cm^2, >0.1 MeV) [32]. The dpa cross sections for W have been obtained from the JENDL4 file (MT444) for the threshold displacement energy of 55 eV, following the recommendation of IAEA [33]. The transmutation of W to Re, Os and Ta according to nuclide inventory calculations, using FISPACT-II code and TENDL-17 nuclear databases, was found around 0.59 at% Re, 1.5×10^{-2} at% Os and 8.9×10^{-3} at% Ta.

Annealing at 1200 ^{o}C for 24 h was performed in a tubular furnace under high vacuum of 10^{-5} mbar using a heating/cooling rate of 10 ^{o}C/min.

2.2 Transmission Electron Microscopy (TEM)

TEM was performed with JEOL 3010 TEM operating at 300 kV. The TEM samples were prepared by cutting the irradiated disks into pieces with a size of about 1.5 × 1.5 × 0.5 mm and then the coupons were mechanically polished using SiC paper with grit sizes of 220, 500, 1200,

2000 and 4000 to achieve 70-100 μm thickness. The coupons were rinsed in ethanol and then glued on 3 mm copper grids with an aperture of 1 mm. Finally, TEM specimens were polished electrochemically with a solution of 1.5 wt.% NaOH in water with an applied voltage of 30 V. The local thickness of the specimen was determined from the convergent beam electron diffraction (CBED) pattern and diffraction pattern. Several measurements in different areas were performed to make sure that the observed microstructure is indeed statistically representative. The average dislocation density was measured following the methodology used in [34]. The overall methodology for the registration of tungsten microstructure was adopted from our earlier works where the same tungsten grades were investigated after plastic deformation and high flux plasma exposure [35, 36, 37, 38].

2.3 Positron Annihilation Spectroscopy

2.3.1 Positron annihilation Lifetime Spectroscopy (PALS)

PALS is a powerful and sensitive method for the investigation of open volume defects with concentrations as low as 10^{-6} in materials [39, 40]. When the positron is implanted in a material, it gets thermalized very fast (~10^{-12} s) and before it annihilates with an electron, it can get trapped into defects. The positron lifetime in a defect is inversely proportional to the electron density seen by the positron. The reduced electron density at an open volume defect site, such as a vacancy, divacancy, dislocation or vacancy cluster, increases the positron lifetime, and the positron lifetime increases as the size of the open volume defect increases.

Positron annihilation lifetime measurements were carried out at room temperature using Ortec® PLS-system. The ^{22}Na radionuclide (from evaporated ^{22}NaCl metallic salt), with a half-life of 959.8 days, encapsulated in 3.6 mg/cm^2 thin polyimide (Kapton®) windows, was used as the positron source with an activity of 100 μCi. The active area of the source is 5 mm. The positron source was sandwiched between two pieces of identical specimens. The 1.274 MeV gamma-ray, indicating a positron emission event, and the two 0.511 MeV gamma rays of the positron annihilation event are detected using fast plastic scintillators coupled with photomultiplier (PM) tubes. The time resolution, i.e. the Full-Width Half Maximum (FWHM) of the prompt spectrum, was measured with ^{60}Co and energy windows set as for ^{22}Na and sample measurements and was found around 280 ps. The detectors were placed at a distance of about 3 mm from the sample. For each spectrum, at least two million counts were collected.

The maximum penetration in tungsten of the positrons emitted by ^{22}Na (545 keV maximum energy) is around 50 μm, which is lower than the samples thickness, i.e. all positrons are annihilated inside the sample. The mean penetration depth of positrons having the mean energy of the ^{22}Na spectrum, i.e. 215 keV, is 11 μm, which is large enough to avoid any surface effects. On the other hand, the two 0.511 MeV gammas emitted during the positron annihilation events have very small absorbance (~10%) by the tungsten material.

The data analysis was performed using PALSfit3 software [41]. The experimental spectra were fitted to the expression of equation [41],

$$S(t) = B + R(t) \otimes \left(I_{src} + I_s \right) = B + R(t) \otimes \left(\sum_{k=1}^{L} I'_k e^{-\lambda_{src,k} t} + \sum_{i=0}^{N} I_i e^{-\lambda_i t} \right) \quad (1)$$

which involves a sum of exponential components referring to the source, I_{src}, and to the sample, I_s, convoluted by the resolution function $R(t)$ (Gaussian function) and the background B. Each component is characterized by two parameters: intensity I_i and lifetime $\tau_i = 1/\lambda_i$, and represents annihilation from a specific defect. The components k refer to air, Kapton® and the source part of the spectrum, while $i = 0$ refers to defect-free material and $i = 1,...,N$ to the different open volume defects of the sample. In this expression, it is assumed that in each defect the positron is annihilated independently of the other defects and the defect-free matrix, i.e. there are no correlations.

Since positrons may annihilate both in the source materials (^{22}NaCl) and the thin foil encapsulating it, and these processes contribute additional lifetime components to the PALS spectrum, it is essential to determine these components in order to obtain reliable values of the lifetimes and intensities of the W investigated samples. To this end, a number of reference well-annealed materials (Al, Co, Ni, Cd and Pb) of high purity (better than 99.99%) were analyzed in order to determine the source parameters. Two source components were considered; one for the annihilations in the ^{22}Na source and Kapton® foil (because of their very similar lifetimes) and another one for the annihilations in the air between the source and the specimen.

In the analysis of all PALS spectra, the resolution function was described by a sum of two Gaussians with FWHM of w_1 and w_2 and relative intensities i_{s1} and i_{s2} and a relative centroid shift t_s. The parameters of the resolution function were treated as fitted parameters for both the analysis of the reference samples and the W irradiated samples. In both cases, the fitted values of all the parameters are in agreement.

The obtained lifetimes of the reference materials were found in very good agreement with the values reported in the literature. The lifetime value of the first source component, $\tau_{src,1}$, comprising the annihilations in the source itself and the surrounding Kapton foil was found (371.0 ± 0.6) ps and it is in good agreement with values reported in the literature (in the range 368 - 386 ps for Kapton and NaCl source in [42, 43], 385 ps for Kapton® in [44]). The second source component, $\tau_{src,2}$, corresponding to the annihilations in the air between the source and the specimen, exhibits a lifetime value of (2.20 ± 0.03) ns and a small intensity of (2.6 ± 0.2) %.

2.3.2 Positron Doppler Broadening Spectroscopy

Positron annihilation spectroscopy (PAS) was used to determine the coincidence Doppler broadening (CDB) spectrum in the irradiated samples. The CDB spectrum provides the momentum distribution of the electrons in the material. Thereby, low momentum is associated to valence/free electrons, which are found near open volumes and high momentum is associated to core electrons, which can be used to determine the chemical environment around a positron-electron annihilation site.

The CDB setup [45,46,47] consists of two movable high-purity Ge detectors (coaxial HPGe detector from Canberra type GC3018) with high-energy resolution (FWHM = 0.8 keV at 122 keV and FWHM = 1.8 keV at 1332 keV) and build-in preamplifier (model 2101P). A digital signal processor (DSP Canberra Model 2060) for each detector and a personal computer with a LabView acquisition board card were used to collect the spectra. Both the electronics (two

detectors and coincidence) as well as the hardware (biological shielding and mobility of the detectors) were optimized to measure highly active specimen with moderate detector dead time (< 20%) and very low background.

The measurements were performed at room temperature using a ^{22}Na positron source. The positron source was sandwiched between two identical samples, such that the fraction of positron annihilations outside the samples is negligible.

The low and high-momentum regions in the CDB spectrum were quantified based on the S- and W-parameters, respectively. The S- and W-parameters were defined as the ratio of low momentum ($|c\ p_L| < 2.5 \times 10^{-3}\ m_0 c$) and high momentum ($15 \times 10^{-3}\ m_0 c < |c\ p_L| < 25 \times 10^{-3}\ m_0 c$) regions in the CDB spectrum to the total region, respectively. Here c denotes the lightspeed, m_0 the electron rest mass and p_L the longitudinal component of the positron-electron momentum along the direction of the γ -ray emission.

2.4 X-Ray Diffraction

The crystalline structure was evaluated by X-ray diffraction (XRD) measurements carried out at room temperature using Bruker D8 diffractometer with a Cu K_α X-ray source, a parallel beam stemming from a Göbbel mirror and a scintillator detector.

2.5 Mechanical Properties

2.5.1 Impulse Excitation Technique

The Impulse Excitation Technique (IET) is a non-destructive dynamic method suitable for determining the elastic properties of materials that are elastic, homogeneous and isotropic [48]. In this work, the Young's modulus, E , the shear modulus, G , and the Poisson ratio, ν , of W bar samples were obtained employing IET [49], using the Buzz-o-Sonic system. For these tests, the disc-shaped specimens were supported by a foam material and excited by a light mechanical impulse. The impulse tool used consisted of a steel ball (2 mm diameter) attached to the end of a thin elastic rod. A microphone located in the vicinity of the sample was used to transmit sound vibrations to the signal processing unit. The first and second natural resonant frequencies $f_{1,2}$ were identified, which in turn were used to calculate the values of $E_{1,2}$ corresponding to these frequencies, using [50]

$$E_{1,2} = \frac{3\pi r^4 f_{1,2}^2 \rho\left(1-\nu^2\right)}{K_{1,2}^2 t^2} \tag{2}$$

where t, r, ρ are the thickness, radius and density of the samples and $K_{1,2}$ are natural geometric factors. ν is calculated according to [50] as a function of t/r and f_1/f_2 , while G is determined from the equation

$$G = \frac{E}{2\left(1-\nu^2\right)} \tag{3}$$

2.5.2 Depth sensing indentation

Depth sensing indentation experiments were performed employing NANOVEA's mechanical tester. The maximum load was set to 3N with a (un)loading rate of 20N/min. A creep time of 200 s was applied in all experiments before starting of the unloading process. The loading rate was selected after a series of indentation tests to achieve stability in the hardness values. The creep time was chosen such as to attain equilibrium conditions, *i.e.* almost no change of the indentation depth. A set of nine indentation tests, spaced by 200 µm, were performed. An optical microscope was used to select the indented area free from visible defects.

The hardness, H, of the samples was calculated using the projected area, A_p, of the residual imprint after the indentation tests determined from its optical microscopy images and the maximum applied force $F_{\max}$ through the equation

$$H = \frac{F_{\max}}{A_p} = \frac{2F_{\max}}{d_{\text{mean}}^2} \tag{4}$$

where d_{mean} is the mean diameter of the residual imprint.

While the indenter is held at constant load, creep phenomena occur, i.e. an increase in penetration depth without an accompanying increase in load is observed. For the comparison of the creep data, the maximum creep penetration depth $h_{cr,\max}$ and the rate for reaching 50 % of the maximum creep depth

$$r_{0.5} = \frac{h_{0.5}}{\tau_{0.5}} \tag{5}$$

were employed, where $h_{0.5}$ and $\tau_{0.5}$ are the half-maximum penetration depth and the time needed for achieving it, respectively.

3 Results and Discussion

3.1 Microstructure

3.1.1 Transmission Electron Microscopy

The main TEM findings are briefly summarized in this section, while the complete TEM study including other irradiation temperatures and tungsten grades is reported in a paper submitted for publication. Figure 1 shows four images to reflect (a) reference microstructure, (b) appearance of dislocation loops, (c) appearance of voids and (d) pattern of voids located near low-angle grain boundary. The initial microstructure was composed of large essentially elongated carrot-like grains, slightly elongated sub-grains with a size of 1-3 µm and dislocation lines with a density of 4.5×10^{12} m^{-2}. An example of such microstructure is presented in Figure 1(a). After irradiation, no considerable change in the appearance of sub-grains was observed. The dislocation line density has however decreased from 4.5×10^{12} down to 1.65×10^{12} m^{-2}.

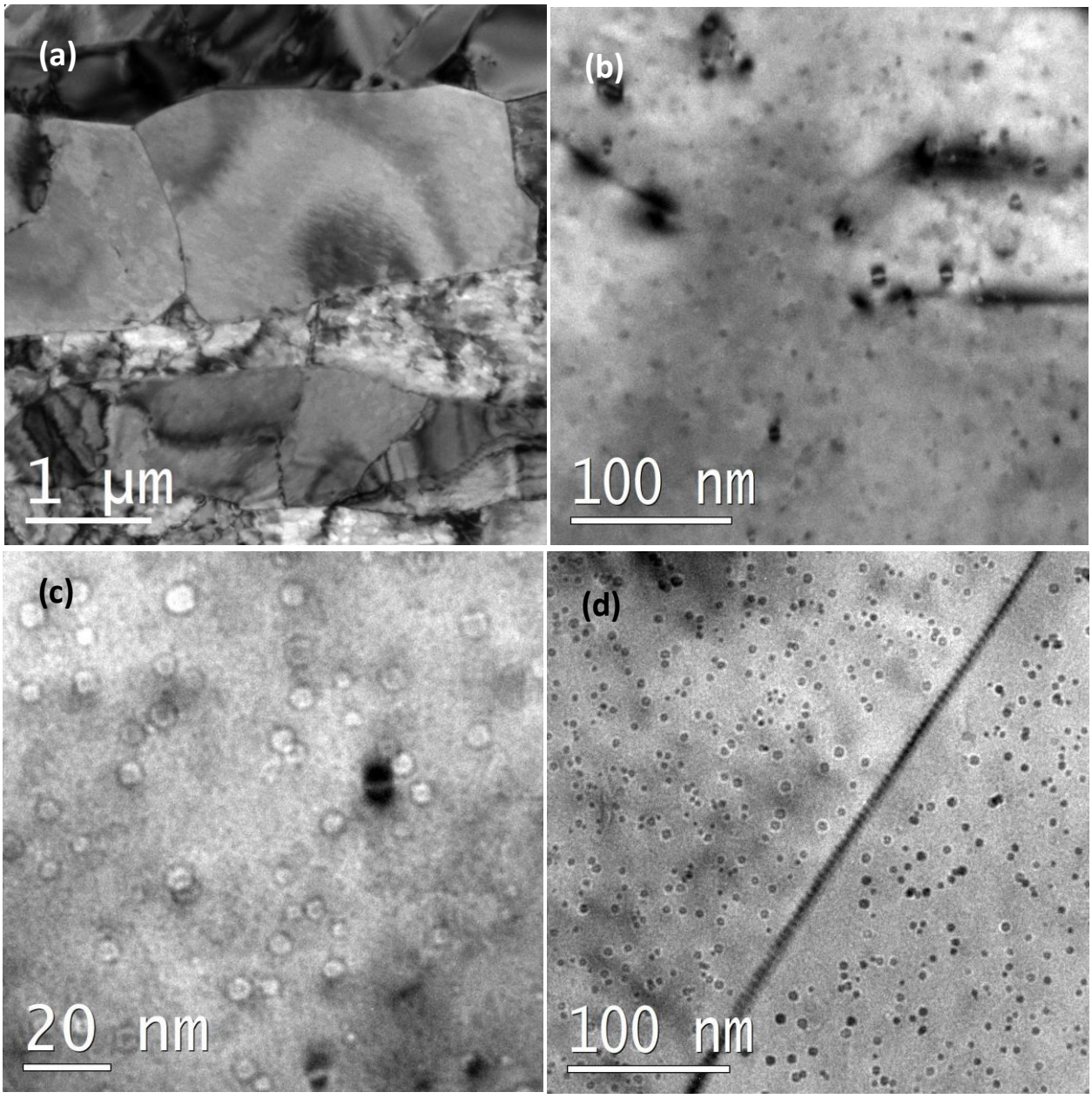

Figure 1. Bright-field TEM images showing (a) reference microstructure; (b) appearance of dislocation loops; (c) appearance of voids; (d) formation of the voids near low-angle grain boundary.

After irradiation, both voids and dislocation loops were identified. The loop size varied from 2.4 up to 13 nm, see Figure 1(b). The void size varied from 1.4 up to 4 nm, see Figure 1(c). The mean size of the voids is 4 nm (density is 1.9×10^{22} m^{-3}) and the mean loop size is around 5.3 nm (density is 5.8×10^{20} m^{-3}). Large voids have faceted shapes. No void lattice could be resolved by performing observations in different orientations with respect to the investigated grain. The region of about 10-30 nm depleted by voids was regularly observed near the grain boundaries, an example is provided in Figure 1(d). Table I summarizes the TEM findings. Although the

irradiation at the high temperature of 1200 °C has resulted in the partial recovery/annihilation of bulk dislocations, the total dislocation line density (i.e. the sum of bulk dislocation and irradiation-induced dislocation loops) has raised from 4.5×10^{12} m^{-2} up to 7.65×10^{12} m^{-2} due to the contribution from the dislocation loops.

Table I. Microstructure determined by TEM measurements.

	Total Dislocation density (lines & loops)	**Dislocation density**	**Dislocation Loops**		**Voids**		
Sample condition	Density ($\times10^{12}$ m^{-2})	Density ($\times10^{12}$ m^{-2})	Density ($\times10^{20}$ m^{-3})	Diameter (nm)	Density ($\times10^{22}$ m^{-3})	Diameter (nm)	Volume fraction (%)
Non-irradiated	4.5	4.5	*	*	-	-	-
Irradiated 1200 °C	7.65	1.65	5.8	3.3	1.9	4	0.07

*Very low density of large dislocation loops (size exceeding 50 nm) was observed in the non-irradiated samples which was attributed to the plastic deformation applied during the forming of the tungsten bar, as reported in our previous work [35,36].

3.1.2 Open Volume defects

3.1.2.1 Positron Lifetime Spectroscopy

PALS measurements were performed on unirradiated, annealed at 1200 °C and irradiated at 1200 °C to a dose of 0.18 dpa W bar, as described in paragraph 2.3. The normalized PALS spectra are presented in Figure 2.

A direct comparison of the experimental spectra of Figure 2 can provide qualitative information on the expected lifetimes. The subtle difference between the unirradiated and the annealed sample, with the latter being at a constantly lower intensity, implies a slightly shorter average lifetime for the annealed sample. For the irradiated sample, the broader peak and the smaller slope compared to the other spectra indicate the appearance of a high lifetime component.

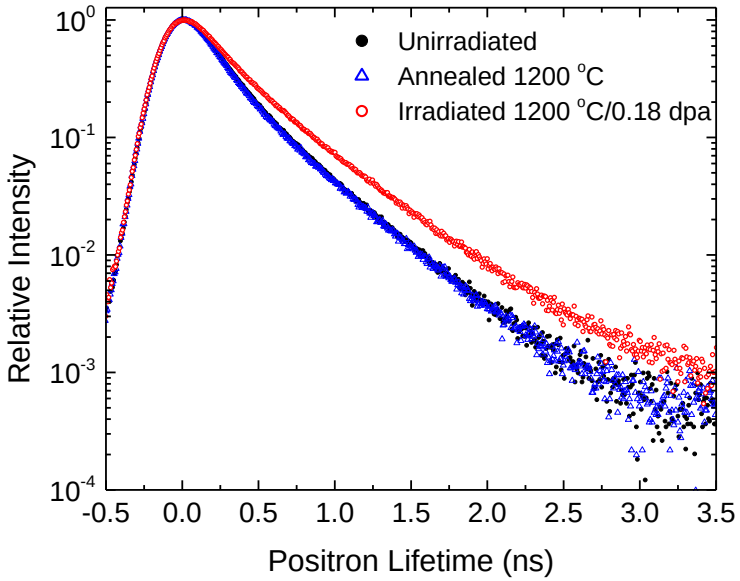

Figure 2. Positron lifetime spectra for unirradiated (•), annealed at 1200 °C for 24 h (△) and irradiated to 0.18 dpa at 1200 °C (○) double forged W bar.

For the unirradiated sample two lifetime components were required in order to fit the PALS spectra. The short lifetime, τ_0, of (114 ± 3) ps and intensity (81 ± 3) % is assigned to annihilations in the bulk defect-free W material (Table II) and is in good agreement with the relevant values reported in the literature which are in the range from 100 to 110 ps [51, 52, 53, 54, 55, 56, 57]. The second lifetime, τ_1, has the value of (250 ± 10) ps and an intensity of (19 ± 3) %. In W, the lifetime for mono- vacancies is reported in the range of 160 to 200 ps and for dislocations in the range of 130 to 180 ps [51, 52, 53, 54, 55, 56, 57, 58, 59]. The vacancy complex of 2-3 vacancies has been found to exhibit a lifetime of 230 ps [52, 60]. Lifetime values from 200 to 380 ps have been reported as equivalent to cluster sizes containing 1 to 9 vacancies [59, 60]. Therefore, τ_1 is considered a weighted average of lifetimes for annihilations taking place at dislocations and small vacancy clusters. The ratio I_1 / I_0 reflects the part of the material which is affected by annihilations at dislocations and small vacancy clusters being of about (23 ± 4)%.

For the fitting of the PALS spectra of the annealed and irradiated sample the lifetime found for the defect-free material was kept constant and equal to that determined for the unirradiated material. For the annealed material the second lifetime was found at (188 ± 8) ps with an intensity (17 ± 2) % (Table II). This lifetime is attributed mainly to dislocations. The decrease of about 60 ps in the τ_1 lifetime after annealing, accompanied by the slight reduction in the average positron lifetime from 139 ps to 127 ps, hints towards vacancy diffusion and recombination with interstitial atoms and/or dislocation rotation/rearrangement. After annealing the ratio I_1 / I_0 decreases slightly reflecting the increase of the annihilations in the defect-free material compared to the unirradiated reference sample (Table II).

Table II. Lifetime components and their relative intensities for unirradiated, annealed at 1200 °C for 24 h and irradiated to 0.18 dpa at 1200 °C double forged W bar.

Sample condition	τ_0 (ps)	τ_1 (ps)	I_1(%)	τ_2 (ps)	I_2(%)	$\tau_{average}$ (ps)	I_1 / I_0	I_2 / I_0
Unirradiated	114 ± 3	250 ± 10	19 ± 3	-	-	139 ± 9	0.23 ± 0.04	-
Annealed 1200 °C		188 ± 8	17 ± 2	-	-	127 ± 5	0.20 ± 0.02	-
Irradiated 1200 °C		190 ± 20	18 ± 3	537 ± 6	38 ± 1	290 ± 10	0.41 ± 0.08	0.86±0.08

After irradiation at 1200 °C, apart from the τ_0 and τ_1 lifetimes a third lifetime, τ_2, is required to fit the data. The obtained lifetimes and their relative intensities are presented in Table II. For τ_1 a value of (190 ± 20) ps is found, similar to that of the annealed sample, and it is associated with annihilations at dislocations. The long lifetime, τ_2, is determined (537 ± 5) ps ps with an intensity of $I_2 = (38 \pm 1)\,\%$. This lifetime corresponds to positron annihilations at large vacancy clusters or voids having more than 40 vacancies [53, 60], with a diameter larger than 1 nm in agreement with TEM results. According to the literature voids having 13-37 vacancies present a lifetime of 410 - 440 ps [54]. For large vacancy clusters (>40 vacancies) theoretical calculations predict a small or no dependence of the positron lifetime on the void size due to the localization of positron at the cavity surface, with a saturation positron lifetime value of around 500 ps [40, 53]. For the irradiated sample, the ratio I_1 / I_0 increases by a factor of about 1.8 compared to the unirradiated material, in excellent agreement with the TEM results which show an increase of about 1.7 in the total dislocation density after irradiation (Table I).

3.1.2.2 Positron Doppler Broadening Spectroscopy

The CDB spectrum provides the momentum distribution of the electrons in the material. Thereby low momentum is associated to valence/free electrons, which are found near open volume. To identify the effect of irradiation and annealing temperature on the CDB spectra, I, they are normalized against the spectrum of unirradiated reference material, I_{ref}. The relative CDB spectra, I/I_{ref}, for the irradiated and annealed material are presented in Figure 3.

For the irradiated material, $I_{\mathrm{irr}}/I_{\mathrm{ref}} > 1$ for $p_L < 4 \times 10^{-3}\, m_0 c$ and $I_{\mathrm{irr}}/I_{\mathrm{ref}} < 1$ for $p_L > 4 \times 10^{-3}\, m_0 c$. For the material annealed at 1200 °C, no significant modifications of the CDB profile are observed. The CDB profile observed for the irradiated material is consistent with the profiles reported in [47,60].

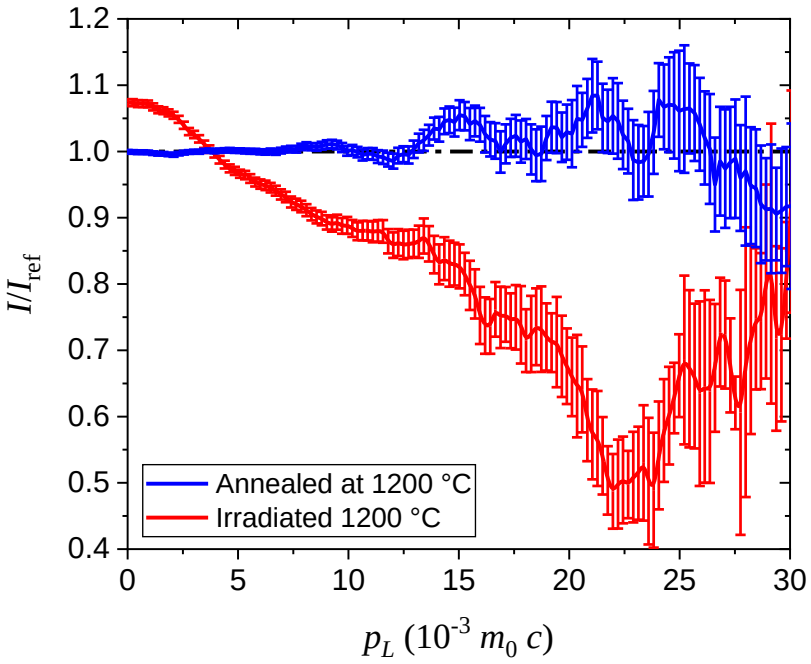

Figure 3. Relative CDB spectra, $I_{\mathrm{irr}}/I_{\mathrm{ref}}$, for the irradiated and annealed samples at 1200 °C. All curves were smoothed by moving average over 10 data points.

The *S*- and *W*-parameters derived from the CDB spectra are presented in Table III. Consistent with the CDS spectra, both *S*- and *W*-parameter for the annealed material are equal to the reference, while for the irradiated sample the S-parameter is 7 % higher, while the *W*-parameter is 3 % lower. The increase in *S*-parameter for the irradiated material is consistent with the creation of open volume defects, such as vacancy clusters and voids. The latter microstructure is consistent with the PALS measurements and TEM data where voids are observed.

Table III. *S*- and *W*-parameters derived from the CDB spectra for the reference, annealed and irradiated materials.

Sample	***S*-parameter**	***W*-parameter**
Unirradiated	0.377 ± 0.001	0.0086 ± 0.0001
Annealed at 1200 °C	0.376 ± 0.001	0.0088 ± 0.0001
Irradiated at 1200 °C	0.402 ± 0.002	0.0058 ± 0.0002

3.1.3 X-Ray Diffractometry

X-Ray diffraction measurements were performed as described in paragraph 2.4 and the spectra are presented in Figure 4. From a direct comparison of the XRD patterns, no new phases are present after annealing or irradiation and the material retains its BCC structure and interatomic distance. Bragg peak broadening appears after irradiation at 0.18 dpa, indicative of the presence of micro-stresses due the creation of defects, with the Full Width at Half Maximum (FWHM) of the (110) peak increasing from 0.126° to 0.19°. After annealing at 1200 °C the FWHM decreases to 0.098° indicating relieving of micro-stresses induced by the forging process. It is observed that after irradiation the relative intensities of the Bragg peaks change, i.e. texture appears. In order to assess the observed texture of the samples, the texture coefficient was utilized, defined as

$$Tc\left(hkl\right)_i = \frac{\frac{I\left(hkl\right)_i}{I_0\left(hkl\right)_i}}{\frac{1}{N}\sum_{i=1}^{N}\frac{I\left(hkl\right)_i}{I_0\left(hkl\right)_i}} \quad (6)$$

where for each crystallographic plane $\left(hkl\right)_i$ its texture coefficient, $Tc\left(hkl\right)_i$, is the ratio of the observed intensity, $I\left(hlk\right)_i$, to the intensity of a randomly oriented polycrystalline sample, $I_0\left(hkl\right)_i$, normalized to the total number of peaks, N, and their respective ratios [61]. A texture coefficient of 1 indicates randomly orientated crystallites, whereas a value higher than 1, a preference in that specific direction.

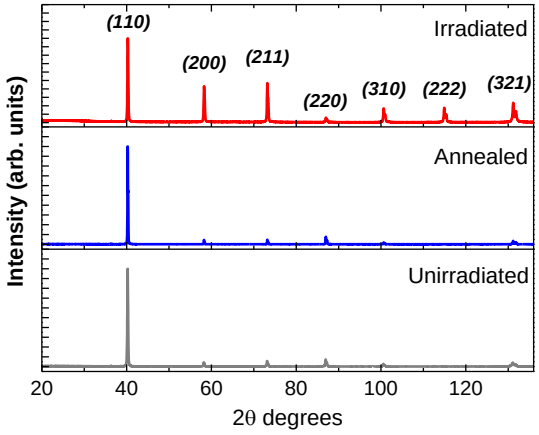

Figure 4. X-Ray diffraction patterns of unirradiated, annealed at 1200 °C for 24 h and irradiated to 0.18 dpa at 1200 °C double forged W bar.

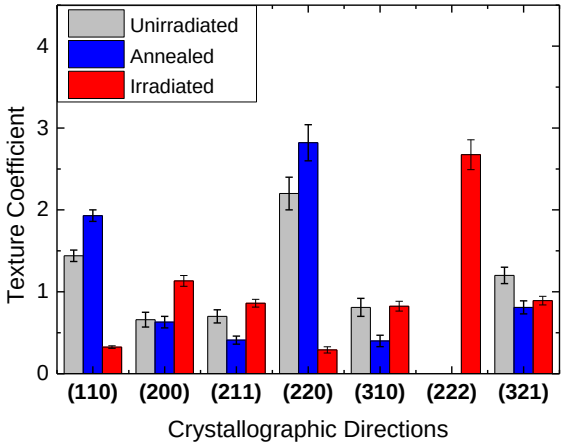

Figure 5. Texture coefficients of each crystallographic direction of unirradiated, annealed at 1200 °C for 24 h and irradiated at 1200 °C double forged tungsten bars.

The texture coefficient is depicted in Figure 5. For the unirradiated material, enhanced texture is observed in the <hh0> direction, produced from the characteristic manufacturing

process of double forging. This preferential texture is retained after annealing at 1200 °C, with insignificant changes, indicating that the recrystallization process has not been activated at that temperature. After irradiation at 1200 °C, a change of texturing is observed, towards the <hhh> direction. Several authors have reported recrystallization in the temperature range of 1100 to 1300 ^{o}C for deformed tungsten materials [27, 28, 62, 63, 64]. The developed texture after recrystallization is highly dependent on the type of deformation and material composition [65], with authors reporting textures similar to the pre-annealed material with increased [63, 64] or decreased [66] intensity, and even recrystallization towards a rotated cube component {001}<110> [67].

3.2 Mechanical Properties

3.2.1 Elastic properties

The Young's, E, and shear, G, moduli and the Poisson's ratio ν were determined as described in section 2.5.1 and they are presented in Table IV. The elastic property values for the unirradiated sample are in a good agreement with the literature data [11, 68]. The material exhibits a 4% increase in the elastic (from 391 to 405 GPa) and shear moduli (from 154 to 158 GPa) after annealing. This increase is attributed to stress-relieving of forging induced stresses and it is in agreement with the PALS data showing a decrease in the part of the material affected by dislocations (see Section 3.1.2.1). A small decrease of 4 % is observed in the elastic (from 391 to 378 GPa) and shear moduli (from 154 to 148 GPa) which indicates the introduction of internal stresses through irradiation.

Table IV. Hardness, maximum creep depth and creep rate, Young's modulus (E), shear modulus (G), Poisson's ratio (ν), for unirradiated, annealed at 1200 °C for 24 h and irradiated to 0.18 dpa at 1200 °C double forged W bar.

Sample condition	Young's Modulus (GPa)	Shear Modulus (GPa)	Poisson's Ratio	Hardness (3 N) (GPa)	Maximum Creep Depth ((nm)	Creep Rate (nm/s)
Unirradiated	391 ± 4	154 ± 1	0.270 ± 0.006	4.40 ± 0.09	319 ± 41	30 ± 2
Annealed 1200 ^{o}C	405 ± 4	158 ± 2	0.286 ± 0.003	4.24 ± 0.04	359 ± 10	37 ± 8
Irradiated 1200 ^{o}C	378 ± 6	148 ± 3	0.280 ± 0.003	5.30 ± 0.14	272 ± 14	33 ± 5

3.2.2 Hardness and creep

Characteristic residual imprints, from which the projected area of indentation was calculated after the indentation tests, are presented in Figure 6. After annealing at 1200 ^{o}C, the phenomenon of thermal grain boundary grooving [69, 70, 71] is observed, revealing the

underlying grain structure. Due to thermally activated surface diffusion, the grain boundaries shrink in order to reduce their surface energy, developing characteristic thermal grooves between individual grains on the surface. In contrast, the surface of the irradiated sample appears rougher but oxide-free.

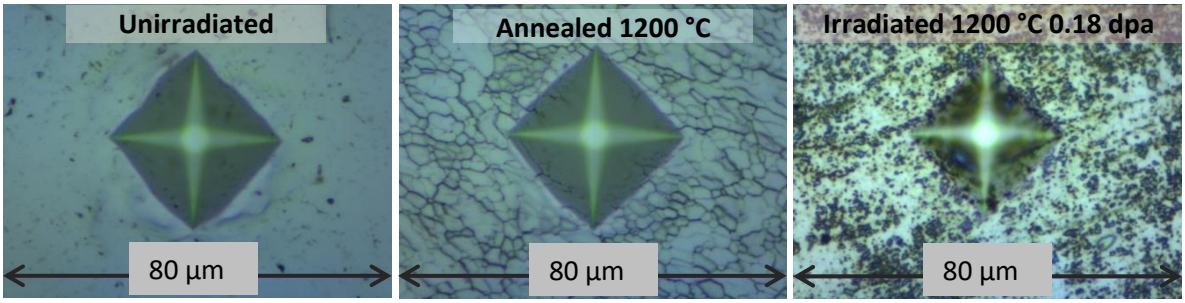

Figure 6. Residual impressions after Vickers indentation tests on unirradiated (left), annealed at 1200 °C for 24 h (middle) and irradiated to 0.18 dpa at 1200 °C (right) double forged W bar.

The creep-time curves under a constant load of 3 N are presented in Figure 7. From these curves, the creep characteristics in Table IV were extracted.

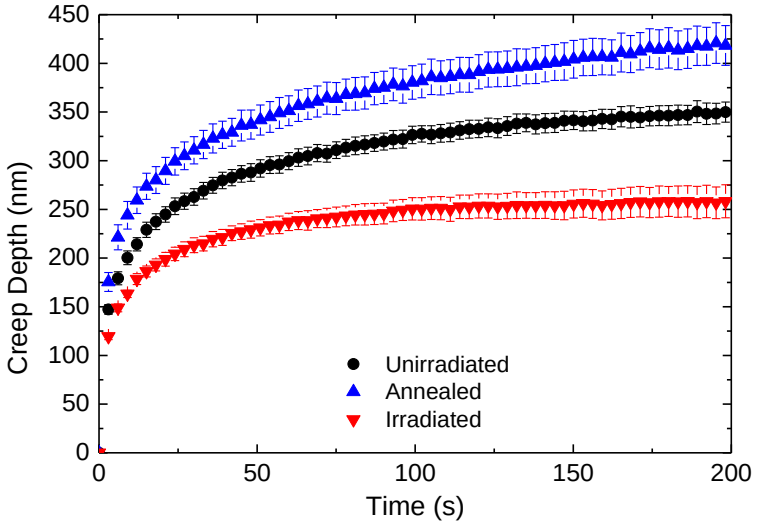

Figure 7. Averaged creep-time curves under a constant load of 3 N of unirradiated (•), annealed at 1200 °C for 24 h (▲) and irradiated to 0.18 dpa at 1200 °C (▼) double forged W bar.

Prior to analysing the creep curves a direct comparison between the curves can be made. Qualitatively, all samples exhibit the same behaviour, with a relatively fast steady-state achieved after 200 s. The higher/lower total creep depth for the annealed/irradiated sample with respect to the unirradiated sample is an indication on the ease/hindering of dislocation movement.

After annealing at 1200 °C hardness decreases by around 4% from 4.4 GPa to 4.24 GPa, while it results in the increase of the maximum creep depth by 13%, indicating facilitation of dislocation movement after partial annealing of forging induced defects, rearrangement of dislocations or sub-grain rotation/coalescence [65]. Similar results reporting a small decrease in hardness from ~4.4 to ~4.3 GPa in double forged W bar [25] and from ~4.1 to ~4.0 GPa in warm rolled W [28] after annealing at 1300 °C and 1200 °C respectively indicate pre-recrystallization recovery. On the other hand, irradiation at 1200 °C increases the hardness by about 20 % from 4.4 GPa to 5.3 GPa, while it decreases the maximum creep depth by 15%, due to irradiation-induced defects that hinder dislocation movement. The creep rate remains largely unaffected after both irradiation and annealing.

4 Summary and Conclusions

In the current work, the microstructure and mechanical properties of double forged W bar as fabricated, annealed at 1200 °C for 24 h and irradiated to 0.18 dpa at 1200 °C were investigated. The as-fabricated tungsten sample is characterized by elongated grains, as a result of the double forging process, and an equivalent grain size of 87.37 μm, with a sub-grain size of 1-3 μm. Forging also introduces dislocations in the material with a density of $N_{disl} = 4.5 \times 10^{12}\,\mathrm{m}^{-2}$ as observed by TEM. Enhanced texture along <hh0> direction is observed in the as fabricated condition. PALS measurements show the presence of a lifetime τ_1 of 250 ps which is attributed to annihilations taking place at small vacancy clusters of 2-3 vacancies and dislocations.

Annealing at 1200 °C results in the decrease of the lifetime τ_1 to 180 ps indicating annihilation of the small vacancy clusters and positron annihilation mainly at dislocations. In addition, reduction of the FWHM of the Bragg XRD peaks is observed. These effects show that the recovery regime of high-temperature treatment is in effect, enabling the diffusion and annihilation of small vacancy clusters, rearrangement and rotation of sub-grains and dislocations. Furthermore this picture of microstructural evolution upon annealing justifies the observed changes on the mechanical properties, i.e. 4% decrease in hardness, 13% increase in the maximum creep depth and 4% increase in the elastic constants.

In the irradiated at 1200 °C material enhanced texture along <222> direction is observed at the expense of <110> orientation while TEM observations do not show any grain growth. Dislocation loop ($N_{loop} = 5.8 \times 10^{20} m^{-3}$, $D = 5.1\,\mathrm{nm}$) and void ($N_{void} = 1.9 \times 10^{22}\ \mathrm{m}^{-3}$, $D = 3.3\,\mathrm{nm}$) formation is observed by TEM after irradiation. Void formation is also suggested by the appearance of a high-intensity long lifetime component ($\tau_2 = 537 \pm 5$ ps) in PALS, corresponding to voids having a size of more than 1 nm, accompanied by the annihilation of small vacancy clusters as indicated by the reduction of the τ_1 lifetime from 250 ps (for the unirradiated sample) to 190 ps. The fact that τ_1 is the same within error bar for the annealed and irradiated at 1200 °C suggests that the main driving force for the dissolution of the small vacancy clusters is the temperature and not the irradiation itself. The formation of voids and dislocation loops at a lesser degree [72] causes hindering in the dislocation movement and result in the increase of

hardness by about 20%. On the other hand the decrease of the dislocation lines from 4.5×10^{12} m^{-2} in the unirradiated state to 1.65×10^{12} m^{-2} after irradiation leads to a decrease of about 4% in the values of the elastic constants. Moreover, the absence of voids near grain boundaries in a region of about 10-30 nm, as observed by TEM, implies that grain boundaries can act as defect sinks. The maximum creep depth, after irradiation at 1200 °C, decreases by 15% due to the formation of irradiation-induced defects (loops and voids) that hinder dislocation movement. The creep rate remains largely unaffected after both irradiation and annealing.

Acknowledgements

This work has been carried out within the framework of the EUROfusion Consortium and has received funding from the Euratom research and training programme 2014-2018 and 2019-2020 under grant agreement No 633053. The views and opinions expressed herein do not necessarily reflect those of the European Commission.

References

[1] R.A. Pitts, S. Carpentier, F. Escourbiac, T. Hirai, V. Komarov, S. Lisgo, A.S. Kukushkin, A. Loarte, M. Merola, A. Sashala Naik, R. Mitteau, M. Sugihara, B. Bazylev, P.C. Stangeby, A full tungsten divertor for ITER: Physics issues and design status, J. Nucl. Mater. 438 (2013) S48–S56. https://doi.org/10.1016/j.jnucmat.2013.01.008.

[2] G. Pintsuk, Tungsten as a Plasma-Facing Material, in: Compr. Nucl. Mater., Elsevier, 2012: pp. 551–581. https://doi.org/10.1016/B978-0-08-056033-5.00118-X.

[3] J. Davis, V. Barabash, A. Makhankov, L. Plöchl, K.. Slattery, Assessment of tungsten for use in the ITER plasma facing components, J. Nucl. Mater. 258–263 (1998) 308–312. https://doi.org/10.1016/S0022-3115(98)00285-2.

[4] V. Philipps, Tungsten as material for plasma-facing components in fusion devices, J. Nucl. Mater. 415 (2011) S2. https://doi.org/10.1016/j.jnucmat.2011.01.110.

[5] J. Riesch, J.Y. Buffiere, T. Höschen, M. Di Michiel, M. Scheel, C. Linsmeier, J.H. You, In situ synchrotron tomography estimation of toughening effect by semi-ductile fibre reinforcement in a tungsten-fibre-reinforced tungsten composite system, Acta Mater. 61 (2013) 7060–7071. https://doi.org/10.1016/j.actamat.2013.07.035.

[6] Q. Wei, H.T. Zhang, B.E. Schuster, K.T. Ramesh, R.Z. Valiev, L.J. Kecskes, R.J. Dowding, L. Magness, K. Cho, Microstructure and mechanical properties of super-strong nanocrystalline tungsten processed by high-pressure torsion, Acta Mater. 54 (2006) 4079–4089. https://doi.org/10.1016/j.actamat.2006.05.005.

[7] H. Kurishita, S. Matsuo, H. Arakawa, S. Kobayashi, K. Nakai, T. Takida, K. Takebe, M. Kawai, Superplastic deformation in W-0.5 wt.% TiC with approximately 0.1 µm grain size, Mater. Sci. Eng. A. 477 (2008) 162–167. https://doi.org/10.1016/j.msea.2007.05.009.

[8] M. Rieth, J. Reiser, B. Dafferner, S. Baumgärtner, The impact of refractory material properties on the helium cooled divertor design, Fusion Sci. Technol. 61 (2012) 381–384. https://doi.org/10.13182/FST12-1T3.

[9] O. Motojima, The ITER project construction status, Nucl. Fusion. 55 (2015) 104023. https://doi.org/10.1088/0029-5515/55/10/104023.
[10] B. Väli, T. Laas, J. Paju, V. Shirokova, M. Paduch, V.A. Gribkov, E. V. Demina, V.N. Pimenov, V.A. Makhlaj, M. Antonov, The experimental and theoretical investigations of damage development and distribution in double-forged tungsten under plasma irradiation-initiated extreme heat loads, Nukleonika. 61 (2016) 169–177. https://doi.org/10.1515/nuka-2016-0029.
[11] C. Yin, D. Terentyev, T. Pardoen, A. Bakaeva, R. Petrov, S. Antusch, M. Rieth, M. Vilémová, J. Matějíček, T. Zhang, Tensile properties of baseline and advanced tungsten grades for fusion applications, Int. J. Refract. Met. Hard Mater. 75 (2018) 153–162. https://doi.org/10.1016/j.ijrmhm.2018.04.003.
[12] J.H. Yu, H. Tanigawa, D. Hamaguchi, T. Nozawa, Mechanical properties of three kinds of ITER-Grade pure tungsten with different manufacturing processes, Fusion Eng. Des. 157 (2020) 111679. https://doi.org/10.1016/j.fusengdes.2020.111679.
[13] V. Philipps, Tungsten as material for plasma-facing components in fusion devices, J. Nucl. Mater. 415 (2011) S2. https://doi.org/10.1016/j.jnucmat.2011.01.110.
[14] R.C. Rau, R.L. Ladd, J. Moteff, Voids in irradiated tungsten and molybdenum, J. Nucl. Mater. 33 (1969) 324–327. https://doi.org/10.1016/0022-3115(69)90029-4.
[15] J.A. Brinkman, On the Nature of Radiation Damage in Metals, J. Appl. Phys. 25 (1954) 961–970. https://doi.org/10.1063/1.1721810
[16] J.T. Buswell, Vacancy damage in heavy ion and neutron-irradiated tungsten, Philos. Mag. 22 (1970) 787–802. https://doi.org/10.1080/14786437008220947.
[17] M.R. Gilbert, J.C. Sublet, Neutron-induced transmutation effects in W and W-alloys in a fusion environment, Nucl. Fusion. 51 (2011). https://doi.org/10.1088/0029-5515/51/4/043005.
[18] M.J. Lloyd, R.G. Abernethy, M.R. Gilbert, I. Griffiths, P.A.J. Bagot, D. Nguyen-Manh, M.P. Moody, D.E.J. Armstrong, Decoration of voids with rhenium and osmium transmutation products in neutron irradiated single crystal tungsten, Scr. Mater. 173 (2019) 96–100. https://doi.org/10.1016/j.scriptamat.2019.07.036.
[19] A. Hasegawa, M. Fukuda, S. Nogami, K. Yabuuchi, Neutron irradiation effects on tungsten materials, Fusion Eng. Des. 89 (2014) 1568–1572. https://doi.org/10.1016/j.fusengdes.2014.04.035.
[20] V.K. Sikka, J. Moteff, Superlattice of voids in neutron-irradiated tungsten, J. Appl. Phys. 43 (1972) 4942–4944. https://doi.org/10.1063/1.1661050.
[21] M. Fukuda, K. Yabuuchi, S. Nogami, A. Hasegawa, T. Tanaka, Microstructural development of tungsten and tungsten-rhenium alloys due to neutron irradiation in HFIR, J. Nucl. Mater. 455 (2014) 460–463. https://doi.org/10.1016/j.jnucmat.2014.08.002.
[22] A. Hasegawa, M. Fukuda, K. Yabuuchi, S. Nogami, Neutron irradiation effects on the microstructural development of tungsten and tungsten alloys, J. Nucl. Mater. 471 (2016) 175–183. https://doi.org/10.1016/j.jnucmat.2015.10.047.
[23] M. Fujitsuka, B. Tsuchiya, I. Mutoh, T. Tanabe, T. Shikama, Effect of neutron irradiation on thermal diffusivity of tungsten-rhenium alloys, J. Nucl. Mater. 283–287 (2000) 1148–1151. https://doi.org/10.1016/S0022-3115(00)00170-7.
[24] L.M. Garrison, Y. Katoh, N.A.P.K. Kumar, Mechanical properties of single-crystal tungsten irradiated in a mixed spectrum fission reactor, J. Nucl. Mater. 518 (2019) 208–225. https://doi.org/10.1016/j.jnucmat.2019.02.050.
[25] L. Tanure, A. Bakaeva, A. Dubinko, D. Terentyev, K. Verbeken, Effect of annealing on microstructure, texture and hardness of ITER-specification tungsten analyzed by EBSD, vickers micro-hardness and

nano-indentation techniques, J. Nucl. Mater. 524 (2019) 191–199. https://doi.org/10.1016/j.jnucmat.2019.07.005
[26] H. Bolt, V. Barabash, W. Krauss, J. Linke, R. Neu, S. Suzuki, N. Yoshida, Materials for the plasma-facing components of fusion reactors, J. Nucl. Mater. 329–333 (2004) 66–73. https://doi.org/10.1016/j.jnucmat.2004.04.005.
[27] K. Tsuchida, T. Miyazawa, A. Hasegawa, S. Nogami, M. Fukuda, Recrystallization behavior of hot-rolled pure tungsten and its alloy plates during high-temperature annealing, Nucl. Mater. Energy. 15 (2018) 158–163. https://doi.org/10.1016/j.nme.2018.04.004.
[28] A. Alfonso, D. Juul Jensen, G.N. Luo, W. Pantleon, Recrystallization kinetics of warm-rolled tungsten in the temperature range 1150-1350 °c, J. Nucl. Mater. 455 (2014) 591–594. https://doi.org/10.1016/j.jnucmat.2014.08.037.
[29] M. Richou, A. Durif, M. Lenci, M. Mondon, M. Minissale, L. Gallais, G. Kermouche, G. De Temmerman, Recrystallization at high temperature of two tungsten materials complying with the ITER specifications, J. Nucl. Mater. 542 (2020) 152418. https://doi.org/10.1016/j.jnucmat.2020.152418
[30] Krimpalis, S., Mergia, K., Messoloras, S., Dubinko, A., Terentyev, D., Triantou, K., Reiser, J., & Pintsuk, G. (2017). Comparative study of the mechanical properties of different tungsten materials for fusion applications. Physica Scripta, 2017(T170). https://doi.org/10.1088/1402-4896/aa9292
[31] M. Wirtz, I. Uytdenhouwen, V. Barabash, F. Escourbiac, T. Hirai, J. Linke, T. Loewenhoff, S. Panayotis, G. Pintsuk, Material properties and their influence on the behaviour of tungsten as plasma facing material, Nucl. Fusion. 57 (2017). https://doi.org/10.1088/1741-4326/aa6938.
[32] D. Pelowitz, J. Durkee, J. Elson, M. Fensin, R. Johns, G. McKinney, S. Mashnik, J. Verbeke, L. Waters, T. Wilcox, MCNPX 2.7.0 Extensions, 2011
[33] M.J. Norgett, M.T. Robinson, I.M. Torrens, A proposed method of calculating displacement dose rates, Nucl. Eng. Des. 33 (1975) 50–54. https://doi.org/10.1016/0029-5493(75)90035-7.
[34] P. Hirsch, A. Howie, R. Nicholson, D.W. Pashley, M.J. Whelan, Microscopy of Thin Crystals, Krieger Publishing Company Malabar, Florida1977
[35] Dubinko, A., Terentyev, D., Bakaeva, A., Verbeken, K., Wirtz, M., & Hernández-Mayoral, M. (2017). Evolution of plastic deformation in heavily deformed and recrystallized tungsten of ITER specification studied by TEM. International Journal of Refractory Metals and Hard Materials, 66, 105–115. http://dx.doi.org/10.1016/j.ijrmhm.2017.03.004
[36] Dubinko, A., Terentyev, D., Bakaeva, A., Pardoen, T., Zibrov, M., & Morgan, T. W. (2017). Effect of high flux plasma exposure on the micro-structural and -mechanical properties of ITER specification tungsten. Nuclear Instruments and Methods in Physics Research, Section B: Beam Interactions with Materials and Atoms, 393, 155–159. https://doi.org/10.1016/j.nimb.2016.10.041
[37] Dubinko, A., Terentyev, D., Bakaeva, A., Hernández-Mayoral, M., De Temmerman, G., Buzi, L., Noterdaeme, J. M., & Unterberg, B. (2017). Sub-surface microstructure of single and polycrystalline tungsten after high flux plasma exposure studied by TEM. Applied Surface Science, 393, 330–339. https://doi.org/10.1016/j.apsusc.2016.09.071
[38] Dubinko, A., Bakaeva, A., Hernández-Mayoral, M., Terentyev, D., De Temmerman, G., & Noterdaeme, J. M. (2016). Microstructural modifications in tungsten induced by high flux plasma exposure: TEM examination. Physica Scripta, 2016(T167). https://doi.org/10.1088/0031-8949/T167/1/014030
[39] L. Dünkel, Topics in Current Physics, Zeitschrift Für Phys. Chemie. 173 (1991) 125–125. https://doi.org/10.1524/zpch.1991.173.Part_1.125.

[40] Eldrup, M., & Singh, B. N. (1997). Studies of defects and defect agglomerates by positron annihilation spectroscopy. Journal of Nuclear Materials, 251, 132–138. https://doi.org/10.1016/S0022-3115(97)00221-3
[41] J. V. Olsen, P. Kirkegaard, M. Eldrup, Analysis of positron lifetime spectra using the PALS fit3 program, AIP Conf. Proc. 2182 (2019) 0–4. https://doi.org/10.1063/1.5135837.
[42] G. Dlubek, A. Sen Gupta, J. Pionteck, R. Häßler, R. Krause-Rehberg, H. Kaspar, K.H. Lochhaas, Glass transition and free volume in the mobile (MAF) and rigid (RAF) amorphous fractions of semicrystalline PTFE: a positron lifetime and PVT study, Polymer (Guildf). 46 (2005) 6075–6089. https://doi.org/10.1016/j.polymer.2005.04.090.
[43] O. V. Ogorodnikova, M. Majerle, V. V. Gann, J. Čížek, P. Hruška, S. Simakov, M. Štefánik, V. Zach, Verification of the theory of primary radiation damage by comparison with experimental data, J. Nucl. Mater. 525 (2019) 22–31. https://doi.org/10.1016/j.jnucmat.2019.07.019.
[44] G.S. Kanda, L. Ravelli, B. Löwe, W. Egger, D.J. Keeble, Positron annihilation lifetime spectroscopy study of Kapton thin foils, J. Phys. D. Appl. Phys. 49 (2015). https://doi.org/10.1088/0022-3727/49/2/025305.
[45] M .J. Konstantinović, G. Bonny, Thermal stability and the structure of vacancy–solute clusters in iron alloys, Acta Mater. 85 (2015) 107–111. https://doi.org/10.1016/j.actamat.2014.11.026.
[46] M.J. Konstantinović, I. Uytdenhouwen, G. Bonny, N. Castin, L. Malerba, P. Efsing, Radiation induced solute clustering in high-Ni reactor pressure vessel steel, Acta Mater. 179 (2019) 183–189. https://doi.org/10.1016/j.actamat.2019.08.028.
[47] G. Bonny, M.J. Konstantinovic, A. Bakaeva, C. Yin, N. Castin, K. Mergia, V. Chatzikos, S. Dellis, T. Khvan, A. Bakaev, A. Dubinko, D. Terentyev, Trends in vacancy distribution and hardness of high temperature neutron irradiated single crystal tungsten, Acta Mater. 198 (2020) 1–9. https://doi.org/10.1016/j.actamat.2020.07.047.
[48] G. Roebben, B. Bollen, A. Brebels, J. Van Humbeeck, O. Van der Biest, Impulse excitation apparatus to measure resonant frequencies, elastic moduli, and internal friction at room and high temperature, Rev. Sci. Instrum. 68 (1997) 4511–4515. https://doi.org/10.1063/1.1148422.
[49] G. Martinček, The determination of poisson's ratio and the dynamic modulus of elasticity from the frequencies of natural vibration in thick circular plates, J. Sound Vib. 2 (1965) 116–127. https://doi.org/10.1016/0022-460X(65)90089-1.
[50] ASTM, Standard Test Method for Dynamic Young ' s Modulus , Shear Modulus , and Poisson ' s Ratio by Sonic Resonance 1, (2013) 1–9. https://doi.org/10.1520/E1875-08.2.
[51] V.S. Subrahmanyam, P.M.G. Nambissan, P. Sen, Helium bubbles in tungsten studied by positron annihilation, Solid State Commun. 89 (1994) 523–527. https://doi.org/10.1016/0038-1098(94)90749-8.
[52] C.L. Dube, P.K. Kulriya, D. Dutta, P.K. Pujari, Y. Patil, M. Mehta, P. Patel, S.S. Khirwadkar, Positron annihilation lifetime measurement and X-ray analysis on 120 MeV Au+7 irradiated polycrystalline tungsten, J. Nucl. Mater. (2015). https://doi.org/10.1016/j.jnucmat.2015.05.029.
[53] T. Troev, E. Popov, N. Nankov, T. Yoshiie, Model calculation of positron states in tungsten containing hydrogen and helium, J. Phys. Conf. Ser. 207 (2010) 012033. https://doi.org/10.1088/1742-6596/207/1/012033.
[54] S. Zhu, Y. Xu, Z. Wang, Y. Zheng, D. Zhou, E. Du, D. Yuan, M. Fukuda, M. Mihara, K. Matsuta, T. Minamisono, Positron annihilation lifetime spectroscopy on heavy ion irradiated stainless steels and tungsten, J. Nucl. Mater. 343 (2005) 330–332. https://doi.org/10.1016/j.jnucmat.2004.11.024.
[55] J. De Vries, Positron Lifetime Technique with Applications in Material Science, 1987.

[56] J. Heikinheimo, K. Mizohata, J. Räisänen, T. Ahlgren, P. Jalkanen, A. Lahtinen, N. Catarino, E. Alves, F. Tuomisto, Direct observation of mono-vacancy and self-interstitial recovery in tungsten, APL Mater. 7 (2019). https://doi.org/10.1063/1.5082150.
[57] A. Yabuuchi, M. Tanaka, A. Kinomura, Short positron lifetime at vacancies observed in electron-irradiated tungsten: Experiments and first-principles calculations, J. Nucl. Mater. 542 (2020). https://doi.org/10.1016/j.jnucmat.2020.152473.
[58] P.E. Lhuillier, M.F. Barthe, P. Desgardin, W. Egger, P. Sperr, Positron annihilation studies on the nature and thermal behaviour of irradiation induced defects in tungsten, Phys. Status Solidi. 6 (2009) 2329–2332. https://doi.org/10.1002/pssc.200982114.
[59] P.M.G. Nambissan, P. Sen, Positron annihilation study of the annealing behaviour of alpha induced defects in tungsten, Radiat. Eff. Defects Solids. 124 (1992) 215–221. https://doi.org/10.1080/10420159208220193.
[60] X. Hu, T. Koyanagi, M. Fukuda, Y. Katoh, L.L. Snead, B.D. Wirth, Defect evolution in single crystalline tungsten following low temperature and low dose neutron irradiation, J. Nucl. Mater. 470 (2016) 278–289. https://doi.org/10.1016/J.JNUCMAT.2015.12.040.
[61] G.B. Harris, X. Quantitative measurement of preferred orientation in rolled uranium bars, London, Edinburgh, Dublin Philos. Mag. J. Sci. 43 (1952) 113–123. https://doi.org/10.1080/14786440108520972.
[62] X.X. Zhang, Q.Z. Yan, C.T. Yang, T.N. Wang, M. Xia, C.C. Ge, Recrystallization temperature of tungsten with different deformation degrees, Rare Met. 35 (2016) 566–570. https://doi.org/10.1007/s12598-014-0315-2.
[63] L. Tanure, D. Terentyev, V. Nikolić, J. Riesch, K. Verbeken, EBSD characterization of pure and K-doped tungsten fibers annealed at different temperatures, J. Nucl. Mater. 537 (2020). https://doi.org/10.1016/j.jnucmat.2020.152201.
[64] K. Wang, H. Sun, X. Zan, U.M. Ciucani, W. Pantleon, L. Luo, Y. Wu, Evolution of microstructure and texture of moderately warm-rolled pure tungsten during annealing at 1300 °C, J. Nucl. Mater. 540 (2020) 152412. https://doi.org/10.1016/j.jnucmat.2020.152412.
[65] A. Rollett, F. Humphreys, G.S. Rohrer, M. Hatherly, Recrystallization and Related Annealing Phenomena, Elsevier, 2004. https://doi.org/10.1016/B978-0-08-044164-1.X5000-2.
[66] F.Z. Xia, H.G. Wei, M.P. Wang, D.H. Zhu, Investigation of normal recrystallization and abnormal recrystallization in pure tungsten sheet by EBSD, Int. J. Refract. Met. Hard Mater. 52 (2015) 98–103. https://doi.org/10.1016/j.ijrmhm.2015.05.009.
[67] J. Reiser, C. Bonnekoh, T. Karcher, W. Pfleging, D. Weygand, A. Hoffmann, Recrystallisation towards a single texture component in heavily cold rolled tungsten (W) sheets and its impact on micromechanics, Int. J. Refract. Met. Hard Mater. 86 (2020) 105084. https://doi.org/10.1016/j.ijrmhm.2019.105084.
[68] R. Lowrie, A.M. Gonas, Single-Crystal Elastic Properties of Tungsten from 24° to 1800°C, J. Appl. Phys. 38 (1967) 4505–4509. https://doi.org/10.1063/1.1709158.
[69] W.W. Mullins, Theory of Thermal Grooving, J. Appl. Phys. 28 (1957) 333–339. https://doi.org/10.1063/1.1722742.
[70] P. Sachenko, J.H. Schneibel, J.G. Swadener, W. Zhang, Experimental and simulated grain boundary groove profiles in tungsten, Philos. Mag. Lett. 80 (2000) 627–631. https://doi.org/10.1080/09500830050134345.
[71] P. Sachenko, J.H. Schneibel, W. Zhang, Effect of faceting on the thermal grain-boundary grooving of tungsten, Philos. Mag. A Phys. Condens. Matter, Struct. Defects Mech. Prop. 82 (2002) 815–829. https://doi.org/10.1080/01418610208243204.

[72] V. Chatzikos, K. Mergia , E. Manios, S. Dellis, D. Papadakis, D. Terentyev, G. Bonny, A. Dubinko, I.E. Stamatelatos and S. Messoloras, Evolution of microstructure in neutron irradiated cold rolled tungsten and its correlation with mechanical properties, Fus. Eng. Design (submitted for publication).